Multi-stable Acoustic Metamaterials with Re-configurable Mass Distribution

Michael J. Frazier[a)]
Department of Mechanical and Aerospace Engineering, University of California, San Diego, California 92093, USA

(Dated: 5 April 2022)

This article proposes a design strategy for acoustic metamaterial lattices which leverages the characteristic multi-stability and kinematic amplification of the internal architecture to realize a re-configurable effective mass distribution, enabling a corresponding frequency band structure of extreme tunability. The approach builds metamaterial lattices from bi-stable elastic elements featuring the typical two-bar inertial amplification mechanism whose deformation axis is uniquely misaligned with that of its elastic support such that the realized amplification is configuration-specific. Conveniently, a change in the configuration does not simultaneously alter the element dimensions and, therefore, the size/shape of the finite metamaterial structure remains constant. Moreover, as the multi-stability and kinematic amplification are each based in geometry, scaling the resulting metamaterial structure is expected to be straightforward. The dynamic performance of 1D/2D metamaterial architectures exhibiting the proposed design strategy is analytically determined via Bloch wave analysis and supported by numerical demonstration of the corresponding finite structures.

I. INTRODUCTION

Over the past decades, metamaterials – whose engineered internal architecture grants unusual or extraordinary macroscopic response – have garnered increasing attention from researchers as the desire to shape material behavior beyond natural limitations (e.g., chemistry) arises within several areas of materials science and engineering[1–3]. In particular, for acoustic metamaterials, the clever design of the small scale architecture – which regulates the propagation of supported mechanical waves – has elicited such exotic properties as negative effective mass[4], stiffness[5], and refractive index[6], and made plausible such fantastic applications as sub-wavelength imaging[7], cloaking[8,9], acoustic computation[10], and topological insulation[11] in addition to wave focusing[12], filtering[13], and guiding[14].

A review of the literature makes apparent that the bulk of reported acoustic metamaterial architectures are passive such that their properties and functions are fixed at fabrication. Nevertheless, a tuning capacity is desirable, not only to allow for adaptation in the face of potentially changing service requirements, but also to expand the range of response, in general. Consequently, in recent years, a number of strategies have been proposed to tune acoustic metamaterials post-fabrication: piezoelectric controllers[15–18], pre-compression[19] and pre-pressure[20], geometric instability[21,22] and multi-stability[23–27], etc. Despite the diversity of approach, most of the previous studies similarly realize tuning via modifications to the stiffness parameter which, in many instances, is by only a few percent without significant (potentially permanent) structural distortion. Moreover, the use of soft constituents is at the expense of load-bearing capacity while that of special, stimuli responsive constituents

necessarily restricts metamaterial architectures to specific compositions. The literature also includes relatively few metamaterial architectures whose tuning capability is based upon mass density redistribution via liquid transport[28–30] which does not necessarily suffer the same shortcomings as the strategies based on variable stiffness; however, scaling such architectures to extreme dimensions may not be practical due to, e.g., the complexity of required plumbing and/or the in inability of the vascular architecture to tolerate the necessary pressures without buckling/rupture. A method of tuning the dynamic response of acoustic metamaterials without resulting in permanent distortion, sacrificing load-bearing capacity or scalability, or relying on particular material constituents remains a challenge which this article aims to address.

The concept of inertial amplification can be idealized in the *inerter*[31], a two-node mechanical element analogous to the spring and viscous dashpot with the property that the equal and opposite force applied at the nodes is proportional to the relative acceleration between them through an effective mass parameter which is, generally, not equal to of its static counterpart. In the context of architected materials, Yilmaz *et al.*[32–34] analytically and numerically investigated the dynamic performance of discrete lattices with embedded levered masses as amplifying elements. The resulting inertial amplification and anti-resonances generated low, wide, and deep gaps in the frequency range of the dispersion band diagram with less added (static) mass than those produced by local resonance. Meanwhile, as inertial amplification is, in part, a geometric manifestation, the scalability of the architecture is unaffected and the composition not restricted to specific material constituents. Moreover, the static stiffness of the system remains constant. In the intervening years, studies on the physics and utility of inertial amplification via levered masses have extended to continuous systems[35,36], non-linear[37,38] and topological[39] effects, and energy harvesting[40]. In addition, the

———————
[a)]Corresponding author email: mjfrazier@ucsd.edu

amplified velocities generated by lever mechanisms has been exploited for extreme dissipation[41]. Yet, despite the aforementioned features which suggest inertially amplified architecture as an excellent foundation upon which to develop a mass-based tuning capacity, no such effort appears in the literature.

Members of a burgeoning class of mechanical metamaterials characterized by multi-stable architectures have demonstrated a tuning capacity with respect to various material parameters – stiffness[23–27], Poisson's ratio[42], coefficient of thermal expansion[43], etc. – stemming from the re-configurability of the internal geometry. Until now, this capacity has not extended to the mass parameter as, short of adding/removing material, re-configuring the internal geometry is insufficient to effect the tuning. In this article, we present a novel implementation of unit cell multi-stability and kinematic amplification to tune the value and distribution of the effective mass within metamaterial architectures by purely geometric means, impacting the wave dispersion response.

The remainder of the article is organized as follows: Section II presents the multi-stable mass-spring element with tunable inertial amplification ability which composes the metamaterial models considered in this article. A discussion of the geometric parameters which track the degree of tunability (i.e., the disparity in amplification between tuned states) is also provided. Section III describes the analytical and numerical methods for evaluating the metamaterial dynamics, and Sec. IV presents the results which illustrate the tunable performance. We demonstrate the concept in one- and two-dimensional metamaterial architectures with a variable mass distribution. Finally, Sec. V concludes the article and suggests avenues for further study.

II. MODEL DESCRIPTION

A. The Multi-stable Potential

Figure 1a presents a blueprint for a discrete mechanical metamaterial with variable inertial amplification capability. The metamaterial unit cell consists of a two-bar mechanism with masses, m and m_a, localized at the left boundary and internal joints, respectively, such that the non-zero relative displacement of the unit cell boundaries results in an amplified displacement for m_a. In addition to the internal joint, the rigid links of lengths, ℓ_1 and ℓ_2, are coupled by a linear spring of stiffness, k, which penalizes the unit cell deformation. The mechanism geometry resembles that which appears in several of the above-cited works related to inertial amplification; however, the specific implementation in this article ensures that the kinematics – therefore, the corresponding inertial amplification – associated with the two stable configurations ($s = 1, 2$) are unique. In this article, the mechanism deformation axis (i.e., line
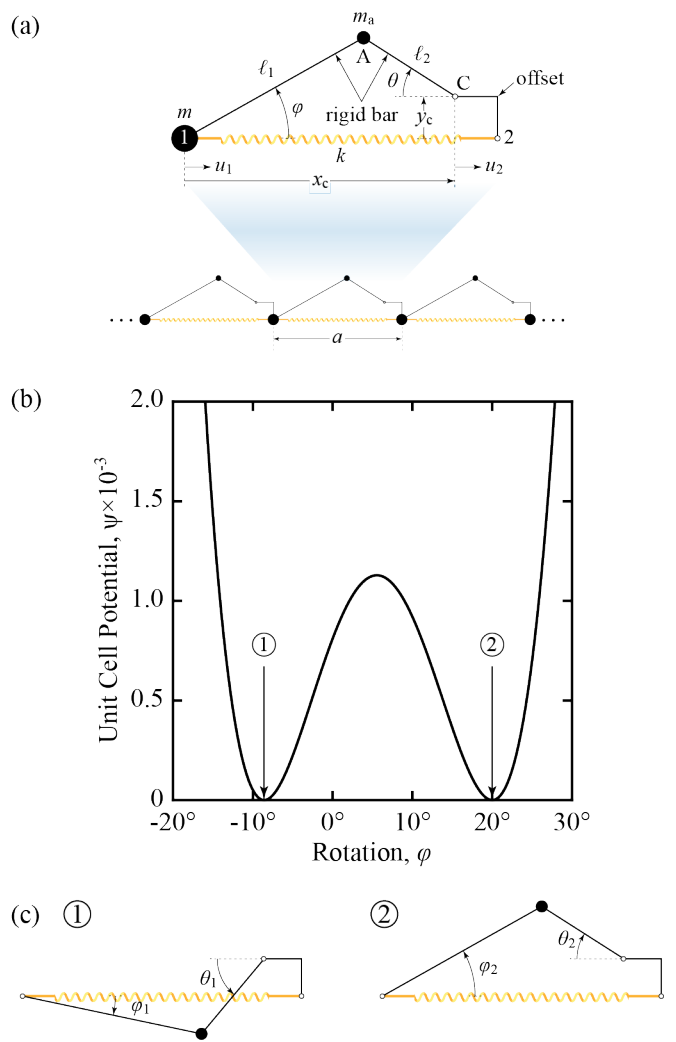

FIG. 1. Multi-stable Metamaterial with Tunable Mass Distribution. (a) Model of multi-stable metamaterial with tunable mass distribution. (b) The unit cell non-convex energy landscape [$k = 10$, $\ell_1 = 1/4$, $\ell_2 = 143/535$, and $(x_c, y_c) = (1/2, 1/20)$] displaying two stable configurations of the bi-stable inertial amplification element. (c) The two stable configurations of the bi-stable element.

through nodes 1 and C) and that of the metamaterial (i.e, lattice vector) are misaligned. The non-convex potential function, ψ (see Appendix), varies with $\varphi \in [0, 2\pi]$, the angle formed by ℓ_1 and the x-axis. This choice of deformation parameters facilitates a visual correlation between the energy diagram in Fig. 1b and the configurations depicted in Fig. 1c. Written explicitly:

$$\psi(\varphi) = \frac{k}{2} \left(\sqrt{\ell_2^2 - [y_c - \ell_1 \sin(\varphi)]^2} - |x_c - \ell_1 \cos(\varphi)| \right)^2,$$
(1)

where, in terms of ℓ_1 and the stable configuration, φ_s,

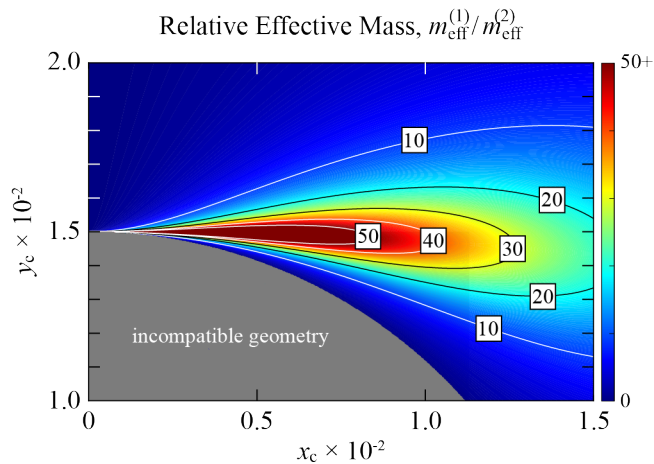$$\ell_2^2 = [x_c - \ell_1 \cos(\varphi_s)]^2 + [y_c - \ell_1 \sin(\varphi_s)]^2.$$

FIG. 2. Effective Mass Disparity. For fixed ℓ_1 and ℓ_2, the location (x_c, y_c) of node C (equivalently, choice of φ_s and θ_s) controls the accessible effective mass associated with each configuration. The above image maps (x_c, y_c) to $m_{\mathrm{eff}}^{(1)}/m_{\mathrm{eff}}^{(2)}$, indicating the factor by which $m_{\mathrm{eff}}^{(1)}$ exceeds $m_{\mathrm{eff}}^{(2)}$. The (x_c, y_c) pairs for which $\ell_1 + \ell_2 < \ell_3$ or $\ell_3 < |\ell_1 - \ell_2|$ are incompatible with the geometry.

For the design, the two degenerate energy minima in Fig. 1b imply that the length of the tuning element in each stable configuration is identical. Although not critical, this feature is beneficial as it permits re-configuring the tuning element without necessitating that the host metamaterial undergo a change in size/shape; eliminating the degeneracy while maintaining the bi-stability, renders the element length configuration-dependent in addition to the inertial amplification. Movie S1 demonstrates the reconfiguration within a 2D system. In the analyses to follow, the small-amplitude dynamics of metamaterials with bi-stable inertia amplification elements (i.e., unit cell in Fig. 1a *sans* mass, m) are assessed about about stable configurations where we adopt the convention, $\varphi_1 < \varphi_2$.

B. Mechanism Equations and Inertial Amplification

The equations governing the dynamics of an isolated unit cell constrained to motion along one dimension emerge from the Lagrangian, $\mathcal{L} = T - V$, where T and V are the kinetic and potential energies of the system, respectively. Specifically,

$$T = \frac{1}{2}m\dot{u}_1^2 + \frac{1}{2}m_a\dot{u}_a^2 + \frac{1}{2}m_a\dot{v}_a^2, \qquad (2a)$$

$$V = \frac{1}{2}k(u_2 - u_1)^2. \qquad (2b)$$

Ultimately, the system configuration is determined by a single degree of freedom such that, for small displacements, the motion of mechanism mass is a linear function of the relative nodal displacement (see Appendix) and the Lagrangian a function of nodal values, i.e., $\mathcal{L}(\mathbf{u}, \dot{\mathbf{u}})$ with $\mathbf{u}^{\mathrm{T}} = [u_1 \quad u_2]$. Applying Lagrange's equations yields the matrix equations of motion, $\mathbf{M}\ddot{\mathbf{u}} + \mathbf{K}\mathbf{u} = \mathbf{0}$, where $\mathbf{M}$ and $\mathbf{K}$ are the system mass and stiffness matrices, respectively:

$$\mathbf{M} = \begin{bmatrix} m + m_a\delta_{11} & -m_a\delta_{12}/2 \\ -m_a\delta_{21}/2 & m_a\delta_{22} \end{bmatrix}, \quad \mathbf{K} = \begin{bmatrix} k & -k \\ -k & k \end{bmatrix}, \quad (3)$$

with coefficients, δ_{ij}, that relate to the configuration of the system:

$$\delta_{11} = [\cos(\varphi_s)\csc(\varphi_s - \theta_s)]^2$$
$$\delta_{12} = \delta_{21} = 2\cos(\varphi_s)\cos(\theta)\cot(\varphi_s - \theta_s)\csc(\varphi_s - \theta_s)$$
$$\delta_{22} = [\cos(\theta_s)\csc(\varphi_s - \theta_s)]^2.$$

Observe, the characteristic inertial coupling between u_1 and u_2 as suggested by the non-zero off-diagonal entries in $\mathbf{M}$. Recognizing that the isolated unit cell possesses only a single non-zero mode of vibration further simplifies the dynamics description to one equation:

$$[m_{\mathrm{st}} + (\delta_{11} + \delta_{12} + \delta_{22} - 1)m_a]\ddot{u} + 4ku = 0, \qquad (4)$$

where the coefficient of $\ddot{u}$ is the effective inertia, m_{eff}, of the system. For the special case in which $\varphi_s = \pi - \theta_s$, Eq. (4) recovers the result obtained by Yilmaz *et al.*[32]. Apparently, although the total static mass of the system is $m_{\mathrm{st}} = m + m_a$, the effective mass can be much larger via δ_{ij} and the outsized influence they provide to even small m_a. The static stiffness as well as the system dimension, a, remain unaffected. Moreover, as the element is bi-stable and δ_{ij} are configuration-specific, so too is m_{eff}; thus, presenting the opportunity for tuning the dynamic response post-fabrication via geometry, i.e., without the need to add/remove material or to invoke stimuli-response elastic constituents. This is especially true for scenarios in which $y_c \neq 0$.

As an illustration of the potential disparity in dynamic response between the two stable configurations, Fig. 2 plots the relative effective mass, $m_{\mathrm{eff}}^{(1)}/m_{\mathrm{eff}}^{(2)}$ (superscript denoting the stable configuration), as a function of (x_c, y_c). Here and in the following, we select $m = 1$, $m_a = 1/10$, $k = 1$, $\ell_1 = 0.115$, and $\ell_2 = 0.100$. Apparently, the bi-stable mechanism can manifest an effective mass in configuration ① that is several times larger than that in configuration ②. The disparity grows as $\varphi_1 \to 0$ and $\varphi_2 \to \pi/2$ simultaneously which, respectively, maximizes the inertial amplification effect in the first configuration while diminishing it in the second. In the remainder of the article, we utilize $(x_c, y_c) = (0.100, 0.015)$ which corresponds to $m_{\mathrm{eff}}^{(1)} = 40.214$ and $m_{\mathrm{eff}}^{(2)} = 1$.

III. DYNAMIC ANALYSIS

We are interested in the post-fabrication adjustable (linear) dynamic response of metamaterial systems for

which the bi-stable element is a key component of the internal architecture. To this end, we consider the time evolution of a small-amplitude disturbance within one- and two-dimensional metamaterial systems using established analytical and numerical techniques.

A. Dispersion Relations

In general, the matrix equations of motion for an arbitrary unit cell about a stable configuration in a discrete or discretized medium are of the form, $\mathbf{M\ddot{u}} + \mathbf{Ku} = \mathbf{f}$, where $\mathbf{f}$ collects the forces applied at the unit cell boundaries by its immediate neighbors. By virtue of the spatially periodic response specified by Bloch theorem, $\mathbf{u}[\boldsymbol{\kappa} \cdot (\mathbf{x} + \mathbf{a}), t] = \mathbf{u}(\mathbf{x}, t)e^{i\boldsymbol{\kappa}\cdot\mathbf{a}}$ with wavevector, $\boldsymbol{\kappa}$, the displacement vector can be condensed to only the essential degrees of freedom, $\mathbf{u}_e$. The wavevector-dependent transformation matrix, $\mathbf{T}$, relates the full and essential sets: $\mathbf{u} = \mathbf{Tu}_e$. Therefore, in terms of $\mathbf{u}_e$, the matrix equations of the periodic medium are $\mathbf{M}_e\mathbf{\ddot{u}}_e + \mathbf{K}_e\mathbf{u}_e = \mathbf{0}$ where $\mathbf{M}_e = \mathbf{T}^H\mathbf{MT}$ and $\mathbf{K}_e = \mathbf{T}^H\mathbf{KT}$ are the energy-consistent condensed mass and stiffness matrices, respectively; $\mathbf{T}^H\mathbf{f} = \mathbf{0}$ maintains that boundary forces do no work and $(\square)^H$ denotes the Hermitian transpose. We assume a time-harmonic response, $\mathbf{u}_e = \mathbf{\tilde{u}}_e e^{i\omega t}$, which establishes an eigenvalue problem in ω^2 with the wavevector-dependent eigenvalues representing the metamaterial-specific frequency dispersion relations.

B. Numerical Analysis

In order to examine the linear response of finite metamaterial structures as well as verify the analytical dispersion results, we simulate the evolution of an initial, localized small-amplitude disturbance in 1D/2D periodic metamaterial systems incorporating the bi-stable element at the unit cell level. The analytical dispersion results are compared to the spatio-temporal Fourier spectrum of the evolved signal. To mitigate the effects of spectral leakage, a Hann window (MATLAB R2021a) with periodic sampling is applied to the signal in both the space and time dimensions. The numerical models incorporate the full non-linear equations of motion. In addition, the models utilize mechanism links of finite stiffness, $k_\ell \gg k$, which introduces additional, predominantly high-frequency modes of oscillation but, otherwise, does not affect the dynamics related to inertial amplification[32]. Here, numerical integration via the Noh-Bathe[44] scheme remains stable for $k_\ell/k = 5000$, although essentially identical results arise for $k_\ell/k = 300$.
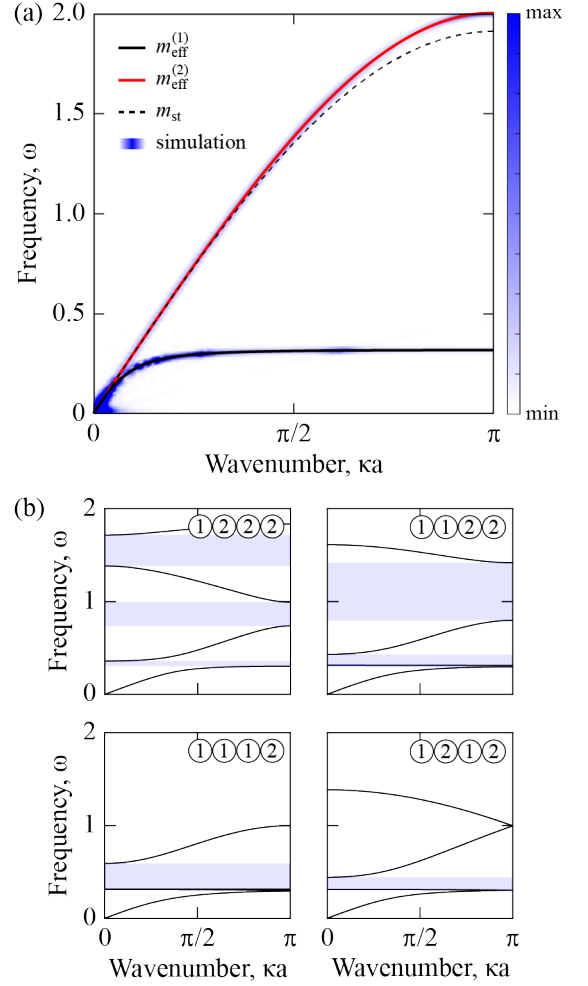

FIG. 3. Frequency Band Structure (1D). (a) Analitycal band structures [Eq. (5)] of 1D metamaterial with uniform effective mass distribution (solid). For reference, the band structure absent amplification (i.e., m_a absorbed into m) is also displayed (dashed). The spatio-temporal Fourier spectra (blue) of a simulated signal in the corresponding finite system. (b) Unique, non-uniform band structures (band gaps shaded) of metamaterial defined by a four-mechanism unit cell. The "stencil", ⓢⓢⓢⓢ, indicates the unit cell mechanism configuration and, thus, the effective mass distribution.

IV. RESULTS AND DISCUSSION

A. 1D Structures

For the scenario depicted in Fig. 1a in which the bi-stable element comprises the unit cell of a one-dimensional metamaterial, $\mathbf{M}$ and $\mathbf{K}$ are provided in Eq. (3), and the application of Bloch's theorem via $\mathbf{T}^T = [1 \quad e^{i\kappa a}]$ yields the characteristic dispersion relation:

$$\omega^2 = \frac{2k[1 - \cos(\kappa a)]}{m_{st} + [\delta_{11} + \delta_{22} - \delta_{12}\cos(\kappa a) - 1]m_a}, \quad (5)$$
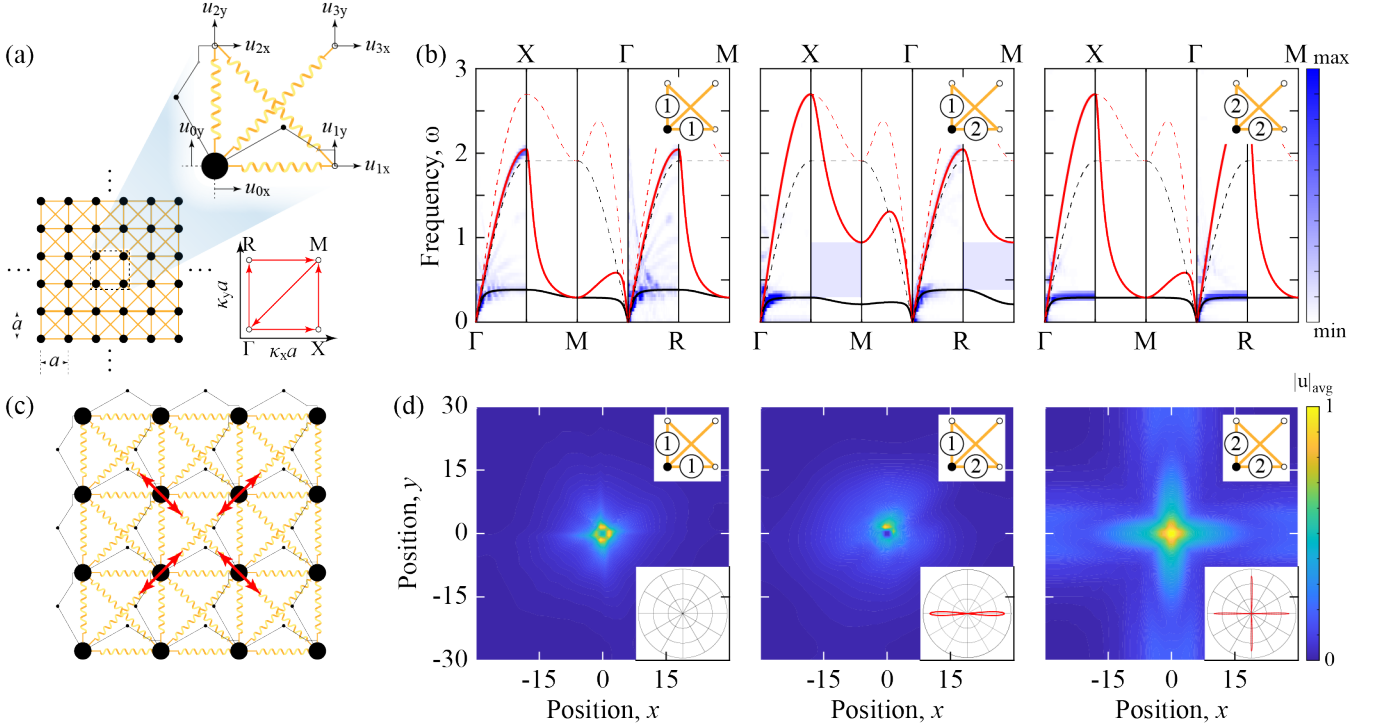
FIG. 4. Frequency Band Structure (2D). (a) Square lattice metamaterial and corresponding unit cell with bi-stable inertial amplification mechanisms. The boundary of the irreducible Brillouin zone is also illustrated. (b) Dispersion diagrams corresponding to unique unit cell configurations indicated by the "stencil" (inset). The spatio-temporal Fourier spectra (blue) of a simulated signal ($\Gamma \rightarrow X$ and $\Gamma \rightarrow R$ directions) in the corresponding finite system. In the anisotropic case, band gaps (shaded regions) separate longitudinal (red, solid) and transverse (black, solid) modes. For comparison, the dispersion curves of the statically equivalent system (dashed) represented by substituting m for $m_{\mathrm{st}} = m + 2m_{\mathrm{a}}$ and removing the amplifying mechanisms. (d) The displacement response of three $30a \times 30a$ systems of unique unit cell configuration with all boundaries free to (c) a centrally-located harmonic dilatation excitation at $\omega = 2.5$. The inset shows directionality of the corresponding group velocity, $v_{\mathrm{g}}(\varphi_{\mathrm{p}})$. The color scaling indicates the magnitude of the local displacement averaged over 20 periods.

which the presence of the δ_{ij} renders configuration-specific. Figure 3a displays the dispersion curves for the metamaterial architecture uniformly in one of the two dynamically unique stable configurations, illustrating a stark difference in response. In each scenario, beyond a maximum frequency, $\omega_{\max}^{(s)}$, a semi-infinite gap opens; however, $\omega_{\max}^{(1)}$ is about a 15% that of $\omega_{\max}^{(2)}$ owing to the factor of forty separating $m_{\mathrm{eff}}^{(1)}$ from $m_{\mathrm{eff}}^{(2)}$. In addition, as $m_{\mathrm{eff}}^{(2)}/m_{\mathrm{st}} = 0.909$, the dispersion curve corresponding to $s = 2$ resembles that of the statically equivalent metamaterial absent inertial amplification (i.e., m_{a} absorbed into m); for $m_{\mathrm{a}} = 0$, the results are, essentially, indistinguishable. These theoretical findings are supported by the Fourier results from simulations of the corresponding non-linear metamaterial structures (1×200 unit cells) following the evolution of an initial, centrally-located displacement perturbation of amplitude, $A = 10^{-4}$. Excellent agreement between the analytical and numerical results is observed.

The configuration-specific frequency range over which the metamaterial supports propagating waves begins to

illustrate the desired dynamics tuning capability, here, through a novel mechanics-based modification of the effective mass rather than the stiffness. Since each bi-stable element within a metamaterial structure can be independently configured, the spatial distribution (periodic or otherwise) of effective mass is extremely customizable and, as consequence, the number of unique dynamic responses extends well beyond those of the two uniform systems described by Eq. (5). For example, 1D periodic systems with two, serially-arranged bi-stable elements per unit cell possess three dynamically unique configurations wherein the frequency range of the band structure may change; three elements permits four unique responses, four yields eight, etc. Since, by design, the static stiffness remains unaltered by changes in configuration, each scenario exhibits identical long-wave sound speed. Moreover, as illustrated in Fig. 3b for a four-element unit cell, a non-uniform effective mass distribution leads to configuration-specific, finite gaps in the frequency range relevant to filtering applications.

B. 2D Structures

Figure 4a shows the unit cell of a square lattice incorporating the bi-stable inertial element along both its horizontal and vertical edges. The corresponding matrices $\mathbf{M}$, $\mathbf{K}$, and $\mathbf{T}$ are provided in the Appendix. Apparently, setting the bi-stable element along each axis to opposite configurations generates an anisotropic mass effect – achieved through the amplification mechanism rather than sub-wavelength resonances[45–48] – as evident by the unequal entries along the main diagonal of $\mathbf{M}$. Such a result may have application in, e.g., mode conversion for nondestructive inspection or the realization of bi-functional lenses[49].

Following the procedure in Sec. III A, we determine the two-dimensional dispersion relations, $\omega(\boldsymbol{\kappa})$, which, accounting for unit cell symmetry, may be tuned to deliver one of three responses (Fig. 4b). Typically, the band diagram is constructed by tracing the boundaries (in reciprocal space) of the irreducible Brillouin zone (IBZ). For the two elements in an identical state, the path $\Gamma \to X \to M \to \Gamma$ delineates the IBZ boundary; however, for the elements in opposite states, the change in unit cell symmetry necessitates an extended path, $\Gamma \to X \to M \to \Gamma \to R \to M$. For a consistent presentation, the diagrams in Fig. 4b adhere to the latter scheme irrespective of unit cell symmetry. In addition, to garner additional insight into the wave dynamics, we compute the group velocity, $\mathbf{v}_{\mathrm{g}} = \nabla\omega$, at particular points on the dispersion surface and plot the results in Fig. 4d; specifically, $v_{\mathrm{g}}(\varphi_{\mathrm{p}})$, where $\varphi_{\mathrm{p}} = \arctan{(\kappa_{\mathrm{y}}/\kappa_{\mathrm{x}})} \in [0, 2\pi]$. The directions of maximum group velocity indicate those most accommodating wave propagation.

Figure 4b shows the frequency dispersion diagrams and supporting Fourier results from simulation – initial displacement perturbation applied at a line of sites bisecting the system across the width and the response measured along a perpendicular line of sites – for the three dynamically unique unit cell configurations of the 2D metamaterial. In each case, the transverse mode is most affected by inertial amplification compared to that in the statically equivalent system. Similarly, regardless of configuration, waves propagating along and about the $\Gamma \to M$ direction experience large frequency downshifts which we attribute to the amplifying elements along each unit cell axis working more effectively in concert. Setting the elements in opposite configurations opens finite band gaps in the $X \to M$ and $R \to M$ directions. Complementing the configuration-dependent dispersion and Fourier results in Fig. 4b, Fig. 4d depicts the time-averaged displacement response of the corresponding finite systems subjected to a harmonic excitation at $\omega = 2.5$. For the finite system with bi-stable elements uniformly in state $s = 1$, a direction-independent semi-infinite band gap prevents radiation away from the point of excitation. For the system with elements uniformly in state $s = 2$, wave propagation is most effective along the $\Gamma \to X$ and $\Gamma \to$
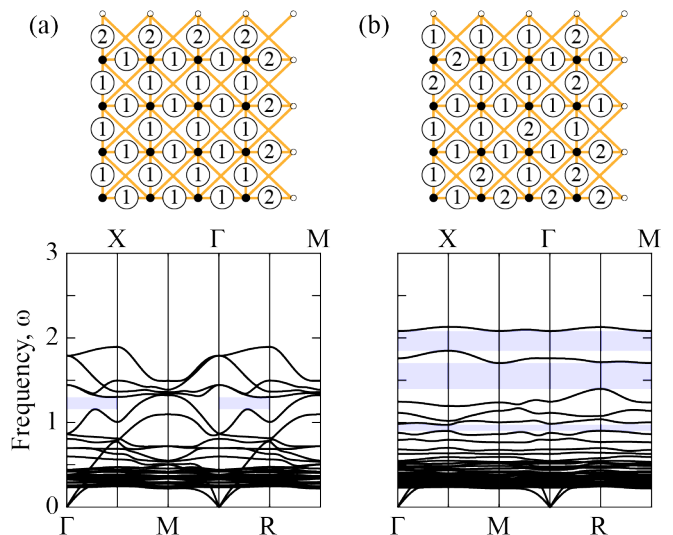

FIG. 5. Extended Unit Cell. (a) Directional and (b) complete band gaps corresponding to unit cells with unique layout of amplifying element configurations (depicted above each diagram).

R directions. These results are supported by the findings in Fig. 4b and the polar plot of v_{g} for $\omega = 2.5$. For the finite system with elements in opposite configurations, wave propagation is expected along only the $\Gamma \to X$ direction; however, the oval-shaped displacement field appears to suggest wave propagation along the $\Gamma \to R$ direction as well, although, slightly less successfully. We attribute this to the anticipated band-gap attenuation being weak in this direction. In Fig. 4b, the Fourier results from simulation match the analytical dispersion results.

Similar to the 1D system, alternative unit cell definitions and element configurations (e.g., the extended cell and morphologies depicted in Fig. 5) may generate different finite band gaps (directional and complete) over various frequency ranges according to the distribution of the bi-stable element configuration; equivalently, the distribution of effective mass. Moreover, prescribing specific configurational patterns within a finite 2D/3D system may yield improvised functional devices (e.g., waveguide)[50]. In some instances, the precise patterning and requisite difference in effective mass between element configurations for specific performance is difficult to know *a priori*. An extensive computational exploration may need be conducted to realize functional devices which operate in the desired frequency ranges.

V. CONCLUSIONS

This article presents a novel implementation of unit cell (geometric) multi-stability and the inertial amplification mechanism to tune the dynamic response of acoustic metamaterials. While there are several

examples in the literature of multi-stability facilitating modifications to the stiffness parameter, here, the effective mass and its distribution are adjusted without an accompanying residual strain (i.e., change to the metamaterial dimensions) or transport of constituent materials. Nevertheless, the mass-focused strategy presented here may work in concert with those earlier stiffness-aimed techniques toward acoustic metamaterials of extreme tunability. However, the presented tuning element lacks the capacity for continuous adjustments possessed by some previously presented designs. While, in this article, attention is restricted to bi-stable unit cells, multi-stable cells may be readily assembled as well (Fig. S1) which may assist in mitigating the effect of the discrete adjustments offered by the presented strategy.

The article analytically and numerically investigates the dynamic characteristics of 1D/2D metamaterial models with embedded bi-stable inertia amplification mechanisms. It is shown that the frequency band structure depends on the specific configurations of the bi-stable mechanisms: opening, sifting, and closing band gaps as well as altering the direction of energy flow. As the number of bi-stable mechanisms per unit cell increase, so to do the number of unique dynamic responses from which to choose. Moreover, in organizing mechanism configurations into mesoscopic patterns, a custom mass distribution is, in effect, achieved. In 2D systems, mechanisms in different states and not identically oriented may give rise to anisotropic effective mass. This is in contrast to the anisotropic mass achieved upon homogenization in metamaterials with sub-wavelength resonances[45–48].

In this article, effecting the multi-stable re-configuration is accomplished mechanically as, for small systems this is a reasonable approach since, except for the rigid-link requirement ($k_a \gg k$), the metamaterial architecture is not reliant on particular material constituents. However, as the number of tuning elements to be manipulated becomes large, practicality favors more the use of active components to assist in the re-configuration. Provided the mechanism is suitably sensitive, any of several environmental fields – electric, magnetic, optical, thermal – may be leveraged to effect the re-configuration. In this manner, active or smart manipulation of acoustic metamaterial dynamics via effective mass tuning is possible.

SUPPLEMENTARY MATERIAL

See the supplementary material for a figure (Fig. S1) related to a multi-stable element with two inertia-amplifying mechanisms and an animation (Mov. S1) demonstrating reconfiguration within a 2D system.

CONFLICT OF INTEREST

The author declares that they have no conflict of interest.

APPENDIX

Potential Function

The potential function, ψ, gives the energy stored by the elastic component of the bi-stable mechanism in relation to the mechanism deformation which, for the particular assembly illustrated in Fig. 1a, can be reflected in any of several configuration parameters. For the dispersion and numerical analysis, the potential is written in terms of the nodal displacements, $\psi(\mathbf{u}) = k(u_1 - u_2)^2/2$; however, for visualizing the non-convex energy landscape and identifying the stable equilibrium configurations, it is necessary that the potential be a function of either φ or θ which are related. Absent the rigid link, the instantaneous length, s, of the line segment separating node A and node C is given by

$$s^2 = [u_2 - u_1 + x_c - \ell_1 \cos(\varphi)]^2 + [y_c - \ell_1 \sin(\varphi)]^2.$$

Upon solving for the relative displacement, $u_2 - u_1$, and substituting the result into $\psi(\mathbf{u})$, the potential is formulated in terms of φ:

$$\psi(\varphi) = \frac{k}{2} \left(\sqrt{s^2 - [y_c - \ell_1 \sin(\varphi)]^2} - |x_c - \ell_1 \cos(\varphi)| \right)^2. \tag{A1}$$

Incorporating the rigid link eliminates s as a variable (i.e., set $s = \ell_2$) and reveals Eq. (A1) to be a function of φ alone. For the mechanism in the stable configuration defined by $\varphi = \varphi_s$, the length of the rigid link is given by:

$$\ell_2^2 = [x_c - \ell_1 \cos(\varphi_s)]^2 + [y_c - \ell_1 \sin(\varphi_s)]^2.$$

Figure 1b plots $\psi(\varphi)$ for the set of material and geometric constants provided in the main text. As discussed in the main, the equi-potential nature of the energy landscape is evidence to the fact that re-configuration does not result in residual deformation of the unit cell.

Notably, provided $y_c \neq 0$ and $\varphi_s \neq \pi - \theta_s$, the mechanism possesses two geometrically unique stable configurations, $\varphi_s = \varphi_{1,2}$, permitting the adjustable inertial amplification factor and metamaterial wave propagation dynamics highlighted in the main. From an energy perspective, $\varphi_s = \varphi_{1,2}$, follow as particular solutions to $\psi'(\varphi) = 0$ for which the stiffness is positive,

i.e., $\psi''(\varphi) > 0$. Geometrically, the stable configurations correspond to the intersections of the circles traced by ℓ_1 and ℓ_2 if free to rotate about node 1 and node C, respectively. By the law of cosines,

$$\varphi_s = \arctan\left(\frac{y_c}{x_c}\right) \pm \arccos\left(\frac{\ell_3^2 + \ell_1^2 - \ell_2^2}{2\ell_1\ell_3}\right), \quad \varphi \in [0, 2\pi], \tag{A2}$$

where $\ell_3^2 = x_c^2 + y_c^2$ and the state, s, is determined following the convention, $\varphi_1 < \varphi_2$. Accordingly,

$$\theta_s = \arctan\left[\frac{\ell_1 \sin(\varphi_s) - y_c}{\ell_1 \cos(\varphi_s) - x_c}\right], \quad \theta_s \in [0, 2\pi]. \tag{A3}$$

The single mechanism presented in the main is restricted to two stable configurations; however, it is conceivable that n additional mechanisms may yield a further $2n$ stable configurations (Fig. S1) and, potentially, as many unique inertial amplification factors. If node 1 and node C are the two foci of an ellipse, then any number of two-link mechanisms may be added to the multi-stable element provided that the link lengths sum to the major axis. Thus, a multi-stable mechanism may realize metamaterials of extreme tunability.

Kinematic Relations

The bi-stable element possesses a single degree of freedom such that the motion of internal node A can be determined in terms of those of external nodes 1 and 2. The following derivations establish these relations for small displacements about an arbitrary stable configuration. Consider the link lengths $\ell_1^2 = (x_a - x_1)^2 + (y_a - y_1)^2$ and $\ell_2^2 = (x_a - x_c)^2 + (y_a - y_c)^2$ from which the corresponding differentials yield:

$$(x_a - x_1)(u_a - u_1) + (y_a - y_1)(v_a - v_1) = 0, \tag{A4a}$$
$$(x_a - x_c)(u_a - u_2) + (y_a - y_c)(v_a - v_2) = 0, \tag{A4b}$$

where the substitutions $dx_i \to u_i$ and $dy_i \to v_i$ are implemented. Recall that node C displaces with node 2 via a rigid connection. Upon solving Eqs. (A4) simultaneously, the desired relations are obtained:

$$u_a = \frac{u_2 - \cot(\varphi_s)\tan(\theta_s)u_1 + \tan(\theta_s)(v_2 - v_1)}{1 - \cot(\varphi_s)\tan(\theta_s)}, \tag{A5a}$$

$$v_a = \frac{u_1 - u_2 + v_1\tan(\varphi_s) - v_2\tan(\theta_s)}{\tan(\varphi_s) - \tan(\theta_s)}. \tag{A5b}$$

For the one-dimensional system, v_1 and v_2 vanish, reducing Eqs. (A5) to the following:

$$u_a = \frac{u_2 - \cot(\varphi_s)\tan(\theta_s)u_1}{1 - \cot(\varphi_s)\tan(\theta_s)}, \tag{A6a}$$

$$v_a = \frac{u_1 - u_2}{\tan(\varphi_s) - \tan(\theta_s)}, \tag{A6b}$$

which, for the special case of $\varphi_s = \pi - \theta_s$, recovers those arrived at in earlier related works[32,35]. Differentiating Eqs. (A6) with respect to time and substituting into Eq. (2a) conveniently reduces the kinetic energy – indeed, the Lagrangian and associated equations of motion – to a function of the u_1 and u_2 alone.

Square Lattice Matrix Equations

For the bi-stable element with motion in the 2D plane, the kinetic energy is given by $T = \frac{1}{2}m\dot{u}_1^2 + \frac{1}{2}m\dot{v}_1^2 + \frac{1}{2}m_a\dot{u}_a^2 + \frac{1}{2}m_a\dot{v}_a^2$. For the moment, consider only the influence of mass, m_a. Upon substitution of the time derivatives of Eqs. (A5) into T, the configuration-specific inertial contribution of m_a is given by $\mathbf{M}_a = \partial_t(\partial_{\dot{\mathbf{u}}}T)$:

$$\mathbf{M}_a = m_a \begin{bmatrix} \delta_{11} & \delta_{12} & -\delta_{13} & -\delta_{14} \\ & \delta_{22} & -\delta_{23} & -\delta_{24} \\ & \text{symm.} & \delta_{33} & \delta_{34} \\ & & & \delta_{44} \end{bmatrix},$$

written consistent with $\mathbf{u}^T = [\mathbf{u}_1 \quad \mathbf{u}_2]$, where $\mathbf{u}_i^T = [u_i \quad v_i]$ and i is the node number. In the preceding,

$$\delta_{11} = [\cos(\varphi_s)\csc(\varphi_s - \theta_s)]^2,$$
$$\delta_{12} = \delta_{21} = \cos(\varphi_s)\sin(\varphi_s)\csc(\varphi_s - \theta_s)^2,$$
$$\delta_{13} = \delta_{31} = \cos(\varphi_s)\cos(\theta_s)\cot(\varphi_s - \theta_s)\csc(\varphi_s - \theta_s),$$
$$\delta_{14} = \delta_{41} = \cos(\varphi_s)\sin(\theta_s)\cot(\varphi_s - \theta_s)\csc(\varphi_s - \theta_s),$$
$$\delta_{22} = [\sin(\varphi_s)\csc(\varphi_s - \theta_s)]^2,$$
$$\delta_{23} = \delta_{32} = \sin(\varphi_s)\cos(\theta_s)\cot(\varphi_s - \theta_s)\csc(\varphi_s - \theta_s),$$
$$\delta_{24} = \delta_{42} = \sin(\varphi_s)\sin(\theta_s)\cot(\varphi_s - \theta_s)\csc(\varphi_s - \theta_s),$$
$$\delta_{33} = [\cos(\theta_s)\csc(\varphi_s - \theta_s)]^2,$$
$$\delta_{34} = \delta_{43} = \cos(\theta_s)\sin(\theta_s)\csc(\varphi_s - \theta_s)^2,$$
$$\delta_{44} = [\sin(\theta_s)\csc(\varphi_s - \theta_s)]^2.$$

Following an assembly process, $\mathbf{M}_a$ is incorporated into the mass matrix, $\mathbf{M}$, of a two-dimensional system. For the square lattice considered in the main, the unit cell $\mathbf{M}$ and $\mathbf{K}$ are given by:

$$\mathbf{M} = m_{\mathrm{a}} \begin{bmatrix} \dfrac{m}{m_{\mathrm{a}}} + \delta_{11}^{\mathrm{h}} + \delta_{22}^{\mathrm{v}} & \delta_{12}^{\mathrm{h}} - \delta_{12}^{\mathrm{v}} & -\delta_{13}^{\mathrm{h}} & -\delta_{14}^{\mathrm{h}} & -\delta_{24}^{\mathrm{v}} & \delta_{23}^{\mathrm{v}} & 0 & 0 \\[2mm] & \dfrac{m}{m_{\mathrm{a}}} + \delta_{11}^{\mathrm{v}} + \delta_{22}^{\mathrm{h}} & -\delta_{23}^{\mathrm{h}} & -\delta_{24}^{\mathrm{h}} & \delta_{14}^{\mathrm{v}} & -\delta_{13}^{\mathrm{v}} & 0 & 0 \\[2mm] & & \delta_{33}^{\mathrm{h}} & \delta_{34}^{\mathrm{h}} & 0 & 0 & 0 & 0 \\[1mm] & & & \delta_{44}^{\mathrm{h}} & 0 & 0 & 0 & 0 \\[1mm] & & & & \delta_{44}^{\mathrm{v}} & -\delta_{34}^{\mathrm{v}} & 0 & 0 \\[1mm] & \text{symm.} & & & & \delta_{33}^{\mathrm{v}} & 0 & 0 \\[1mm] & & & & & & 0 & 0 \\[1mm] & & & & & & & 0 \end{bmatrix},$$

$$\mathbf{K} = \frac{k}{2} \begin{bmatrix} 3 & 1 & -2 & 0 & 0 & 0 & -1 & -1 \\ & 3 & 0 & 0 & 0 & -2 & -1 & -1 \\ & & 3 & -1 & -1 & 1 & 0 & 0 \\ & & & 1 & 1 & -1 & 0 & 0 \\ & & & & 1 & -1 & 0 & 0 \\ & \text{symm.} & & & & 3 & 0 & 0 \\ & & & & & & 1 & 1 \\ & & & & & & & 1 \end{bmatrix},$$

consistent with $\mathbf{u}^{\mathrm{T}} = [\mathbf{u}_0 \quad \mathbf{u}_1 \quad \mathbf{u}_2 \quad \mathbf{u}_3]$. Coefficients, δ_{ij}^{h} and δ_{ij}^{v}, pertain to the bi-stable elements along the horizontal and vertical edges of the unit cell, respectively. For $\mathbf{u}_{\mathrm{e}}^{\mathrm{T}} = [u_0 \quad v_0]$, the corresponding Bloch transformation matrix is given by:

$$\mathbf{T} = \begin{bmatrix} 1 & 0 \\ 0 & 1 \\ \lambda_{\mathrm{x}} & 0 \\ 0 & \lambda_{\mathrm{x}} \\ \lambda_{\mathrm{y}} & 0 \\ 0 & \lambda_{\mathrm{y}} \\ \lambda_{\mathrm{x}}\lambda_{\mathrm{y}} & 0 \\ 0 & \lambda_{\mathrm{x}}\lambda_{\mathrm{y}} \end{bmatrix}$$

where $\lambda_{\mathrm{x}} = \mathrm{e}^{\mathrm{i}\kappa_{\mathrm{x}} a}$ and $\lambda_{\mathrm{y}} = \mathrm{e}^{\mathrm{i}\kappa_{\mathrm{y}} a}$.

DATA AVAILABILITY

[1] M. Maldovan, "Sound and heat revolutions in phononics," *Nature*, vol. 503, pp. 209–217, November 2013.

[2] M. I. Hussein, M. J. Leamy, and M. Ruzzene, "Dynamics of phononic materials and structures: historical origins, recent progress, and future outlook," *Appl. Mech. Rev.*, vol. 66, p. 040802, May 2014.

[3] D. M. Kochmann and K. Bertoldi, "Exploiting microstructural instabilities in solids and structures: from metamaterials to structural transitions," *Appl. Mech. Rev.*, vol. 69, p. 050801, September 2017.

[4] Z. Yang, J. Mei, M. Yang, N. H. Chan, and P. Sheng, "Membrane-type acoustic metamaterial with negative dynamic mass," *Physical Review Letters*, vol. 101, p. 204301, November 2008.

[5] N. X. Fang, D. Xi, J. Xu, M. Ambati, W. Srituravanich, C. Sun, and X. Zhang, "Ultrasonic metamaterials with negative modulus," *Nature Materials*, vol. 5, pp. 452–456, June 2006.

[6] C. M. Park and S. H. Lee, "Zero-reflection acoustic metamaterial with a negative refractive index," *Sci. Rep.*, vol. 9, p. 3372, March 2019.

[7] M. Ambati, N. Fang, C. Sun, and X. Zhang, "Surface resonant states and superlensing in acoustic metamaterials," *Physical Review B*, vol. 75, p. 195447, May 2007.

[8] S. A. Cummer and D. Schurig, "One path to acoustic cloaking," *New J. Phys.*, vol. 9, p. 45, March 2007.

[9] N. Stenger, M. Wilhelm, and M. Wegener, "Experiments on elastic cloaking in thin plates," *Physical Review Letters*, vol. 108, p. 014301, January 2012.

[10] O. R. Bilal, A. Foehr, and C. Daraio, "Bistable metamaterial for switching and cascading elastic vibrations," *Proc. Natl. Acad. Sci.*, vol. 114, pp. 4603–4606, May 2017.

[11] H.-W. Dong, S.-D. Zhao, R. Zhu, Y.-S. Wang, L. Cheng, and C. Zhang, "Customizing acoustic dirac cones and topological insulators in square lattices by topology optimization," *J. Sound Vib.*, vol. 493, p. 115687, February 2021.

[12] H. Danawe, G. Okudan, D. Ozevin, and S. Tol, "Conformal gradient-index phononic crystal lens for ultrasonic wave focusing in pipe-like structures," *Appl. Phys. Lett.*, vol. 117, p. 021906, July 2020.

[13] G. Trainiti, Y. Xia, J. Marconi, G. Cazzulani, A. Erturk, and M. Ruzzene, "Time-periodic stiffness modulation in elastic metamaterials for selective wave filtering: theory and experiment," *Phys. Rev. Lett.*, vol. 122, p. 124301, March 2019.

[14] Y. Pennec, B. Djafari-Rouhani, J. O. Vasseur, A. Khelif, and P. A. Deymier, "Tunable filtering and demultiplexing in phononic crystals with hollow cylinders," *Physical Review E*, vol. 69, p. 046608, April 2004.

[15] B.-J. Kwon, J.-Y. Jung, D. Lee, K.-C. Park, and I.-K. Oh, "Tunable acoustic waveguide based on vibro-acoustic metamaterials with shunted piezoelectric unit cells," *Smart Mater. Struct.*, vol. 24, p. 105018, October 2015.

[16] P. Celli and S. Gonella, "Tunable directivity in metamaterials with reconfigurable cell symmetry," *Appl. Phys. Lett.*, vol. 106, p. 091905, March 2015.

[17] F. Li, C. Zhang, and C. Liu, "Active tuning of vibration and wave propagation in elastic beams with periodically placed piezoelectric actuator/sensor pairs," *J. Sound Vib.*, vol. 393,

pp. 14–29, April 2017.

[18] G. Wang, J. Cheng, J. Chen, and Y. He, "Multi-resonant piezoelectric shunting induced by digital controllers for subwavelength elastic wave attenuation in smart metamaterial," *Smart Mater. Struct.*, vol. 26, p. 025031, February 2017.

[19] C. Daraio, V. F. Nesterenko, E. B. Herbold, and S. Jin, "Tunability of solitary wave properties in one-dimensional strongly nonlinear phononic crystals," *Phys. Rev. E*, vol. 73, p. 026610, February 2006.

[20] H. Dong and Y. Hu, "Harnessing fluid pre-pressure to tune the properties of phononic crystals," *Extreme Mech. Lett.*, vol. 34, p. 100582, January 2020.

[21] K. Bertoldi and M. C. Boyce, "Mechanically triggered transformations of phononic band gaps in periodic elastomeric structures," *Phys. Rev. B*, vol. 77, p. 052105, February 2008.

[22] C. R. Tipton, E. Han, and T. Mullin, "Magneto-elastic buckling of a soft cellular solid," *Soft Matter*, vol. 8, pp. 6880–6883, June 2012.

[23] M. J. Frazier and D. M. Kochmann, "Band gap transmission in periodic bistable mechanical systems," *J. Sound Vib.*, vol. 388, pp. 315–326, February 2017.

[24] J. Meaud and K. Che, "Tuning elastic wave propagation in multistable architected materials," *Int. J. Solids Struct.*, vol. 122–123, pp. 69–80, September 2017.

[25] J. Meaud, "Multistable two-dimensional spring-mass lattices with tunable band gaps and wave directionality," *J. Sound Vib.*, vol. 434, pp. 44–62, November 2018.

[26] Z. Wu, Y. Zheng, and K. W. Wang, "Metastable modular metastructures for on-demand reconfiguration of band structures and nonreciprocal wave propagation," *Phys. Rev. E*, vol. 97, p. 022209, February 2018.

[27] V. Ramakrishnan and M. J. Frazier, "Multistable metamaterial on elastic foundation enables tunable morphology for elastic wave control," *J. Appl. Phys.*, vol. 127, p. 225104, June 2020.

[28] Q. Zhang, K. Zhang, and G. Hu, "Tunable fluid-solid metamaterials for manipulation of elastic wave propagation in broad frequency range," *Appl. Phys. Lett.*, vol. 112, p. 221906, June 2018.

[29] T.-T. Wang, Y.-F. Wang, Y.-S. Wang, and V. Laude, "Tunable fluid-filled phononic metastrip," *Appl. Phys. Lett.*, vol. 111, p. 041906, July 2017.

[30] Y.-F. Wang, T.-T. Wang, Y.-S. Wang, and V. Laude, "Reconfigurable Phononic-Crystal Circuits Formed by Coupled Acoustoelastic Resonators," *Phys. Rev. Applied*, vol. 8, p. 014006, July 2017.

[31] M. C. Smith, "Synthesis of mechanical networks: the inerter," *IEEE Trans. Autom. Control*, vol. 47, pp. 1648–1662, October 2002.

[32] C. Yilmaz, G. M. Hulbert, and N. Kikuchi, "Phononic band gaps induced by inertial amplification in periodic media," *Phys. Rev. B*, vol. 76, p. 054309, August 2007.

[33] C. Yilmaz and G. Hulbert, "Theory of phononic gaps induced by inertial amplification in finite structures," *Phys. Lett. A*, vol. 374, pp. 3576–3584, July 2010.

[34] G. Acar and C. Yilmaz, "Experimental and numerical evidence for the existence of wide and deep phononic gaps induced by inertial amplification in two-dimensional solid structures," *J. Sound Vib.*, vol. 332, pp. 6389–6404, November 2013.

[35] N. M. M. Frandsen, O. R. Bilal, J. S. Jensen, and M. I. Hussein, "Inertial amplification of continuous structures: large band gaps from small masses," *J. Appl. Phys.*, vol. 119, p. 124902, March 2016.

[36] F. Zeighami, A. Palermo, and A. Marzani, "Inertial amplified resonators for tunable metasurfaces," *Meccanica*, vol. 54, pp. 2053–2065, October 2019.

[37] J. Zhou, L. Dou, K. Wang, D. Xu, and H. Ouyang, "A nonlinear resonator with inertial amplification for very low-frequency flexural wave attenuations in beams," *Nonlinear Dyn.*, vol. 96, pp. 647–665, April 2019.

[38] V. Settimi, M. Lepidi, and A. Bacigalupo, "Nonlinear dispersion properties of one-dimensional mechanical metamaterials with inertia amplification," *Int. J. Mech. Sci.*, vol. 201, p. 106461, July 2021.

[39] H. B. Al Ba'ba'a, X. Zhu, and Q. Wang, "Enabling novel dispersion and topological characteristics in mechanical lattices via stable negative inertial coupling," *Proc. R. Soc. A*, vol. 477, p. 20200820, August 2021.

[40] S. Adhikari and A. Banerjee, "Enhanced low-frequency vibration energy harvesting with inertial amplifiers," *J. Intell. Mater. Syst. Struct.*, p. 1045389X211032281, August 2021.

[41] H. B. Al Ba'ba'a, Z. Lin, and S. T. Tol, "Metadamping enhancement and tunability via scissor-like electromechanical metamaterials," *J. Appl. Phys.*, vol. 130, p. 184901, November 2021.

[42] H. Yang and L. Ma, "Angle-dependent transitions between structural bistability and multistability," *Adv. Eng. Mater.*, vol. 22, p. 1900871, May 2020.

[43] H. Yang and L. Ma, "1D to 3D multi-stable architected materials with zero Poisson's ratio and controllable thermal expansion," *Materials & Design*, vol. 188, p. 108430, March 2020.

[44] G. Noh and K.-J. Bathe, "An explicit time integration scheme for the analysis of wave propagations," *Comput. Struct.*, vol. 129, pp. 178–193, August 2013.

[45] R. Zhu, Y. Chen, Y. S. Wang, G. K. Hu, and G. Huang, "A single-phase elastic hyperbolic metamaterial with anisotropic mass density," *J. Acoust. Soc. Am.*, vol. 139, pp. 3302–3309, June 2016.

[46] R. Zhu, H. Yasuda, G. Huang, and J. Yang, "Kirigami-based elastic metamaterials with anisotropic mass density for subwavelength flexural wave control," *Sci. Rep.*, vol. 8, January 2018.

[47] M. Jaberzadeh, B. Li, and K. T. Tan, "Wave propagation in an elastic metamaterial with anisotropic effective mass," *Wave Motion*, vol. 89, pp. 131–141, June 2019.

[48] X. Yang, Y. Chai, and Y. Li, "Metamaterial with anisotropic mass density for full mode-converting transmission of elastic waves in the ultralow frequency range," *AIP Adv.*, vol. 11, p. 125205, December 2021.

[49] R. Zhu, C. Ma, B. Zheng, M. Y. Musa, L. Jing, Y. Yang, H. Wang, S. Dehdashti, N. X. Fang, and H. Chen, "Bifunctional acoustic metamaterial lens designed with coordinate transformation," *Appl. Phys. Lett.*, vol. 110, p. 113503, March 2017.

[50] N. Yang, C.-W. Chen, J. Yang, and J. L. Silverberg, "Emergent reconfigurable mechanical metamaterial tessellations with an exponentially large number of discrete configurations," *Mater. Des.*, vol. 196, p. 109143, November 2020.